Computers & Geosciences 135 (2020) 104399

Contents lists available at ScienceDirect

Computers and Geosciences

journal homepage: www.elsevier.com/locate/cageo

Research paper

A generalized poroelastic model using FEniCS with insights into the Noordbergum effect

Ryan Haagenson [a,*], Harihar Rajaram [b], Jeffery Allen [c]

[a] Civil, Environmental, and Architectural Engineering, University of Colorado Boulder, 1111 Engineering Dr, 422 UCB, Boulder, CO, 80309, USA
[b] Environmental Health and Engineering, Johns Hopkins University, 615 N Wolfe St, Baltimore, MD, 21205, USA
[c] Computational Science Center, National Renewable Energy Laboratory, 15013 Denver West Pkwy, Golden, CO, 80401, USA

ARTICLE INFO

Keywords:
Poroelasticity
Geomechanics
FEniCS
DOLFIN
Model development

ABSTRACT

Understanding the coupled behavior of fluid flow and solid deformation in porous media is often a critical aspect of geoscientific investigations, including studies of injection-induced seismicity, geological carbon sequestration, or surface deformation from pumping operations. In 1941, Biot first outlined the standard poroelastic formulation that accounted for this coupling within an isotropic and elastic porous medium. This fully coupled system of partial differential equations typically requires the use of numerical modeling for any practical purposes, necessitating either lengthy code development or the use of a complex, prebuilt model that often lacks flexibility. However, due to recent advances in automated approaches to solving systems of differential equations, problems of poroelasticity can now be easily handled in a streamlined yet flexible manner. Here, we present a poroelastic model built within the framework of FEniCS – an open source, general purpose finite element method software – which solves the system monolithically and can produce a continuous and mass-conserving solution for specific discharge. We present both a linear model and a generalized, nonlinear model. The nonlinear model allows for variable fluid density and employs a fluid pressure and volumetric strain dependent porosity relationship. The behavior of the linear model is verified with common benchmark problems, whereas results from the nonlinear model are compared to assess the impact of including its generalizations. Finally, the model is applied to a two-dimensional problem of fluid extraction meant to replicate the well-known Noordbergum effect (in which the fluid pressure in layers adjacent to the pumped layer temporarily increases during pumping). This is often referred to as "reverse water fluctuation". This showcases not only the flexibility of the model but also its ability to simulate numerically challenging scenarios. The results from this simulation suggest a novel explanation of the physical mechanism generating the Noordbergum effect: strain gradients.

1. Introduction

Although many subsurface problems can be sufficiently represented with an uncoupled formulation (e.g. standard groundwater flow theory or soil mechanics), a fully coupled poroelastic formulation is often required. For instance, problems related to induced seismicity, geological carbon sequestration, or surface deformation from pumping operations all require a detailed understanding of the coupled hydro-mechanical behavior of the subsurface. Biot (1941) established the foundation of linear poroelasticity theory, which provides a framework for coupling fluid flow and solid deformation. Since Biot's work, numerous derivations of poroelasticity have been presented with varying forms and poroelastic constants (Biot, 1941, 1962; Cheng, 2016; Coussy, 2004; Detournay and Cheng, 1993; Geertsma, 1957; Verruijt, 2013; Wang, 2000).

Typically, numerical simulations of poroelastic problems require solving a system of fully coupled partial differential equations in terms of four dependent field variables (i.e. fluid pressure and the three components of solid displacement) with associated constitutive relationships. In general, if a model parameter (such as porosity or fluid density) is assumed to vary with fluid pressure and volumetric strain, the coupled system of equations is rendered nonlinear. Solving this transient, nonlinear, fully coupled formulation is a nontrivial task, which requires a complex numerical approach. Hence, traditional model development in a high-level language requires extensive, time-consuming, and error-prone code development. Ferronato and Gambolati (2010) have published an open-source code of this variety.

A growing number of large-scale general subsurface flow simulators can model poroelastic systems, some of which are open-source. Both

* Corresponding author.
E-mail address: ryan.haagenson@colorado.edu (R. Haagenson).

https://doi.org/10.1016/j.cageo.2019.104399
Received 25 July 2019; Received in revised form 2 December 2019; Accepted 3 December 2019
Available online 6 December 2019
0098-3004/

TOUGH-FLAC (Rutqvist, 2010) and MOOSE (Gaston et al., 2009) are popular subsurface modeling platforms with hydro-mechanical capabilities. Researchers at Los Alamos National Laboratory have recently developed hydro-mechanical capabilities in PFLOTRAN as well (Karra et al., 2013). While these prebuilt models provide tremendous benefit to the geoscientific community, the user's control over many aspects of the model is generally limited. Model components including the governing equations, function spaces, and nonlinear terms are typically preset; altering these would require a detailed understanding of the large and multifaceted code.

Automated approaches for solving systems of partial differential equations – such as FEniCS – provide a unique alternative to both traditional code development and prebuilt models mentioned above. FEniCS is an open source, general-purpose finite element method software available as a C++ or Python library (Alnaes et al., 2015). With FEniCS, the user gains a great deal of control over many model aspects while the bulk of the finite element code (i.e. assembling the matrices and solving the system) is easily handled by various FEniCS functions. Therefore, FEniCS offers a more streamlined approach than traditional code development but also more flexibility than a prebuilt model.

Though FEniCS has been used in a wide range of research contexts, it has only recently grown in popularity for geoscientific applications including fluid flow in heterogeneous porous media (Srinivasan and Rajagopal, 2016), dissolution of carbon dioxide in soils (Unwin et al., 2016), and heat convection in the mantle (Zhang et al., 2016). Following this trend, we present a numerical model for fully coupled poroelasticity developed using the FEniCS framework. Although some previous works have developed poroelastic models using FEniCS (Kolesov et al., 2014; Zhang et al., 2015), they have not made the code freely available. Moreover, we expand upon these models in numerous ways. The model presented here allows the solid grains to be compressible, allows for a variable fluid density, defines a fluid pressure and volumetric strain dependent porosity relationship, and employs a mixed finite element approach to solve the system monolithically. A monolithic approach to poroelastic problems has been shown by others to avoid numerical "locking" (or spurious, non-physical oscillations in the fluid pressure and solid displacement solutions) (Ferronato and Gambolati, 2010). These generalizations are easily accommodated by the FEniCS framework. In fact, many generalizations are possible with FEniCS, including using a different flow law, mechanical constitutive relationship, or introducing additional nonlinearities.

The subsequent sections discuss the mathematical and numerical model, including a rigorous derivation of the porosity relationship and the model's implementation within FEniCS. Next, results from two poroelastic benchmark problems – Terzaghi's and Cryer's problems – are presented to verify the model's behavior. Finally, the model is used to show that strain gradients rather than volumetric strains appear to be the physical mechanism driving the Noordbergum effect, which showcases the model's flexibility and usefulness.

2. Governing equations

This section presents the equations governing fluid flow and solid deformation in a coupled poroelastic formulation. Note that all primary variables are treated as perturbations from the initial static condition (i.e. either the hydrostatic or lithostatic condition) (Biot, 1941; Cheng, 2016; Verruijt, 2013; Wang, 2000). Fluid flow and deformation of the porous media is generated by fluid pressure or stress state perturbations from this initial condition. In this form, gravity completely disappears from the equations and both initial and boundary conditions become very simple to apply. Following an approach similar to that of Verruijt (2013), the continuity equation for poroelasticity can be derived by starting with the fluid continuity equation in a porous medium written as

$$\frac{\partial \left(\rho_f \phi\right)}{\partial t} + \nabla \cdot \left(\rho_f \phi \vec{v}_f\right) = f_f \tag{1}$$

where ρ_f is the fluid density, ϕ is the porosity, $\vec{v}_f$ is the fluid velocity, and f_f is the source or sink term for fluid. Fluid velocity, $\vec{v}_f$, is related to specific discharge through Darcy's law:

$$\vec{q} = \phi\left(\vec{v}_f - \vec{v}_s\right) = -\frac{\kappa}{\mu}\nabla p \tag{2}$$

where $\vec{q}$ is the specific discharge, $\vec{v}_s$ is the solid grain velocity, κ is the intrinsic permeability of the porous medium, μ is the dynamic viscosity of the fluid, and p is the fluid pressure perturbation from the hydrostatic condition. Note that this is the rigorous form of Darcy's law that accounts for the relative velocity between the fluid and solid grains.

Some formulations – such as those used in TOUGH-FLAC, MOOSE, PFLOTRAN, or the models developed by Cappa and Rutqvist (2011) and Vilarrasa et al. (2013, 2014) – use continuity in its most general form given by Eq. (1) where the storage term is left as $\partial(\rho_f\phi)/\partial t$. However, standard poroelastic formulations expand the storage term similar to Biot's (1941) original work, which is the approach we have taken here. Substituting Eq. (2) into Eq. (1) and expanding gives

$$\rho_f \frac{\partial \phi}{\partial t} + \phi \frac{\partial \rho_f}{\partial p}\frac{\partial p}{\partial t} + \rho_f \phi \frac{\partial \epsilon_v}{\partial t} + \nabla \cdot \left(\rho_f \vec{q}\right) = f_f. \tag{3}$$

In going from Eq. (1) and Eq. (2) to Eq. (3), $\nabla \cdot \vec{v}_s$ is assumed equal to $\partial\epsilon_v/\partial t$, where ϵ_v is the volumetric strain of the porous medium by use of a small strain approximation. The $\vec{v}_s \cdot \nabla\left(\rho_f\phi\right)$ term is assumed to be negligible and is therefore dropped. The second term in Eq. (3) can be simplified by supplying an equation of state, relating fluid density to fluid pressure. For example, a common equation of state for a liquid is

$$\rho_f(p) = \rho_0 \exp\left(\beta_f\left(p + p_S - p_0\right)\right) \tag{4}$$

where ρ_0 and p_0 are the reference fluid density and pressure respectively, p_S is the initial hydrostatic fluid pressure distribution, and β_f is the fluid compressibility. In this case, the second term in Eq. (3) can be rewritten as

$$\phi \frac{\partial \rho_f}{\partial p}\frac{\partial p}{\partial t} = \phi \rho_f \beta_f \frac{\partial p}{\partial t}. \tag{5}$$

However, the model can handle any equation of state supplied by the user, including compressible gases. For this reason, the second term of Eq. (3) is left in general form.

If using the continuity equation given in Eq. (1), then an expression relating porosity to the various hydraulic or mechanical variables is required. Similarly, we require a porosity relationship in order to convert Eq. (3) to the standard poroelastic formulation. Numerous porosity relationships have been previously suggested, such as the Palmer–Mansoori model, Settari–Mourits model, empirical models, or models chosen for convenience (Cappa and Rutqvist, 2011; Fang et al., 2013; Hou et al., 2012; Karra et al., 2013; Liu et al., 2015; Palmer and Mansoori, 1998; Rutqvist, 2010; Settari and Mourits, 1998; Zhang et al., 2008). However, these porosity relationships are inconsistent with standard poroelasticity and are more concerned with capturing certain physical behaviors. To derive the standard form of poroelasticity, we must employ a porosity relationship based on solid continuity (Verruijt, 2013). The solid continuity equation can be written as

$$\frac{\partial \rho_s(1-\phi)}{\partial t} + \nabla \cdot \left(\rho_s(1-\phi)\vec{v}_s\right) = 0 \tag{6}$$

where ρ_s is the density of the solid grains. Assuming the solid grains are isotropic, elastic solids in isothermal conditions, their density can be expressed in terms of fluid pressure and volumetric strain of the porous medium with

$$\frac{\partial \rho_s}{\partial t} = \frac{\rho_s \beta_s}{1-\phi}\left((\alpha - \phi)\frac{\partial p}{\partial t} - \frac{1}{\beta_m}\frac{\partial \epsilon_v}{\partial t}\right) \tag{7}$$

where β_s is the solid grain compressibility, $\alpha = 1 - \beta_s/\beta_m$ is Biot's coefficient, and β_m is the compressibility of the porous medium (Biot and Willis, 1957; Fall et al., 2014; Rutqvist et al., 2001; Verruijt, 2013).

Eq. (7) inherently assumes that stress is positive in compression following the typical convention in geomechanics (Verruijt, 2013; Wood, 1991; Zoback, 2010). Substituting Eq. (7) into Eq. (6) and rearranging gives

$$\frac{\partial \phi}{\partial t} = (\alpha - \phi)\left(\beta_s \frac{\partial p}{\partial t} + \frac{\partial \epsilon_v}{\partial t}\right). \tag{8}$$

Integrating Eq. (8) produces the porosity relationship used in this model, written as

$$\phi\left(p, \epsilon_v\right) = \alpha - \left(\alpha - \phi_0\right)\exp\left(-\left(\epsilon_v + \beta_s p\right)\right) \tag{9}$$

where ϕ_0 is the initial porosity in an unperturbed, static state with the effects of gravity included. This porosity relationship does not account for the effects of damage or failure, which are often neglected in poroelastic formulations.

Substituting Eq. (8) into Eq. (3) produces the final form of the continuity equation — where the $\rho_f \phi\, \partial \epsilon_v / \partial t$ term can be canceled:

$$\rho_f \alpha \frac{\partial \epsilon_v}{\partial t} + \left(\rho_f (\alpha - \phi)\beta_s + \phi \frac{\partial \rho_f}{\partial p}\right)\frac{\partial p}{\partial t} + \nabla \cdot \left(\rho_f \vec{q}\right) = f_f. \tag{10}$$

This is the commonly used continuity equation in standard poroelastic formulations, where the storage term has now been expanded into two terms instead of left in the general form seen in Eq. (1). (Biot, 1941; Cheng, 2016; Geertsma, 1957; Verruijt, 2013; Wang, 2000). Even though a porosity relationship was required to derive Eq. (10), both porosity and fluid density are often treated as constants creating a linear system of equations (Biot, 1941; Chang and Segall, 2016; Cheng, 2016; Ferronato and Gambolati, 2010; Gambolati et al., 2000; Geertsma, 1957; Verruijt, 2013; Wang, 2000). This simplified approach is required for obtaining analytical solutions to many poroelastic problems but also sufficiently represents any problem where fluid density and porosity changes are negligible. We also present a generalized model that allows for variable fluid density and employs the porosity relationship given in Eq. (9), involving a dependence on fluid pressure and volumetric strain. In this paper, the first and second approaches are referred to as the "linear" and "nonlinear" models respectively.

It is clear from the rigorous derivation of Eq. (10), that the same porosity relationship used in the derivation should also be used to describe the evolution of porosity wherever it appears in the mathematical model — maintaining internal consistency. Any other porosity relationship (including those listed above) would produce a mathematically inconsistent formulation. Note that some models already employ this internally consistent approach (e.g. MOOSE (Gaston et al., 2009), Fall et al. (2014), and Vilarrasa et al. (2013, 2014)).

The equations for linear elasticity complete the poroelastic formulation. First, the equation for mechanical equilibrium is given as

$$\nabla \cdot \boldsymbol{\sigma} = \vec{0} \tag{11}$$

where $\boldsymbol{\sigma}$ is a tensor representing the stress state perturbation from the lithostatic condition. Effective stress, $\boldsymbol{\sigma}'$, is given by Biot's general definition, written as

$$\boldsymbol{\sigma} = \boldsymbol{\sigma}' + \alpha p \boldsymbol{I} \tag{12}$$

where $\boldsymbol{I}$ is the second rank identity tensor. Here, again, stresses are taken as positive in compression, following typical geomechanics convention (Verruijt, 2013; Wood, 1991; Zoback, 2010). The linear constitutive model between stress and strain can be written as

$$\boldsymbol{\sigma}' = -2G\boldsymbol{\epsilon} - \left(K - \frac{2}{3}G\right)\epsilon_v \boldsymbol{I} \tag{13}$$

where $\boldsymbol{\epsilon}$ is the strain tensor, G is the shear modulus, and $K = 1/\beta_m$ is the bulk modulus of the porous medium. Strain is related to solid displacement, $\vec{u}$, by the expression

$$\boldsymbol{\epsilon} = \frac{1}{2}\left(\nabla \vec{u} + \left(\nabla \vec{u}\right)^T\right). \tag{14}$$

Finally, we can define the volumetric strain of the porous medium (using a small strain approximation) as

$$\epsilon_v = \nabla \cdot \vec{u} = tr(\boldsymbol{\epsilon}). \tag{15}$$

The final governing equations for the model presented here are continuity, Darcy's law, and mechanical equilibrium given by Eq. (2), (10) and (11) respectively. This formulation has seven primary unknowns: fluid pressure (p), the three components of specific discharge ($\vec{q}$), and the three components of solid displacement ($\vec{u}$). The model's mechanical component is completed with Eqs. (12) through (15), which are each defined separately from Eq. (11) in the model's code. An equation of state (such as Eq. (4)) and the porosity relationship (given in Eq. (9)) provide the appropriate constitutive relationships, leading to a generalized, nonlinear poroelastic formulation.

3. Numerical model

In the mixed finite element scheme, the interpolated solutions for fluid pressure (p_h), specific discharge ($\vec{q}_h$), and solid displacement ($\vec{u}_h$) are given by the summations:

$$p_h = \sum_{i=1}^{n_{elem}} N_i^p \, p_{elem} \tag{16}$$

$$\vec{q}_h = \sum_{i=1}^{n_{face}} N_i^q \, \vec{q}_{face} \tag{17}$$

$$\vec{u}_h = \sum_{i=1}^{n_{node}} N_i^u \, \vec{u}_{node} \tag{18}$$

where n_j denotes the number of mesh entities of jth type, N_i^x is the ith shape function for the variable x, and x_j is the solution value of the variable x at the jth type of mesh entity.

In three dimensions, the physical domain (written as Ω) and the domain boundary (written as Γ) are discretized into tetrahedral elements and triangular facets respectively. Suitable function spaces that satisfy the inf–sup condition for well posedness in poroelasticity are given by

$$\hat{P}_h = \{p \in L^2(\Omega)\} \tag{19}$$

$$\hat{Q}_h = \{\vec{q} \in H(div) : \vec{q} \cdot \vec{n} = q_{BC} \text{ on } \Gamma_F\} \tag{20}$$

$$\hat{U}_h = \{\vec{u} \in H^1(\Omega) : \vec{u} = \vec{u}_{BC} \text{ on } \Gamma_D\} \tag{21}$$

where $\hat{P}_h$, $\hat{Q}_h$, and $\hat{U}_h$ are the function spaces for fluid pressure, specific discharge, and solid displacement respectively, $\vec{n}$ is the outward normal vector of the mesh facets, Γ_F is the stipulated flux boundary, and Γ_D is the stipulated displacement boundary (Brezzi et al., 1985; Brezzi and Fortin, 1991; Ferronato and Gambolati, 2010). Note that traction and pressure boundary conditions are applied through the weak form of the governing equations, shown in Section 3.1. Here, $L^2(\Omega)$, $H(div)$, and $H^1(\Omega)$ are well-known Sobolev spaces (Adams and Fournier, 2003; Kirby et al., 2012). As others have shown, a stable combination of finite element types for these function spaces is the piecewise constant element for fluid pressure, the lowest-order Brezzi–Douglas–Marini (BDM) element for specific discharge, and the continuous linear element for solid displacements (Ferronato and Gambolati, 2010; Zhang et al., 2015). The BDM element was developed for second-order elliptical equations, and therefore has a natural fit with flow in porous media (Brezzi et al., 1985). Coupled with the piecewise constant element for pore fluid pressure, the BDM element produces a continuous and mass-conserving solution for specific discharge (Ferronato and Gambolati, 2010; Traverso et al., 2013).

The time derivatives of volumetric strain and fluid pressure in Eq. (10) are discretized with a backward Euler scheme to keep the numerical model fully implicit. To handle the nonlinearities (i.e. fluid density and porosity), the model employs a Picard iteration where the efficiency and stability are enhanced by under-relaxation. Picard iteration was selected over alternatives for solving nonlinear systems of differential equations, such as various Newton–Krylov methods, because of its ease in implementation and consistently robust performance in solving this particular formulation of nonlinear poroelasticity.

3.1. Weak forms of the governing equations

The weak forms of the governing equations were derived using a traditional Galerkin method. Below, we use superscripts k and $k+1$ to denote the current and next time levels and superscripts m and $m+1$ to denote the current and new Picard iterates. Multiplying Eq. (2), (10) and (11) by the respective test functions for fluid pressure (P_T), specific discharge ($\vec{Q}_T$), and solid displacement ($\vec{U}_T$), integrating over Ω, and rearranging gives the final weak form:

Find $p^{k+1,m+1} \in \hat{P}_h$, $\vec{q}^{\,k+1,m+1} \in \hat{Q}_h$, and $\vec{u}^{\,k+1,m+1} \in \hat{U}_h$ such that

$$\begin{aligned}
&\int_\Omega \rho_f^{k+1,m} \alpha \epsilon_v^{k+1,m+1} P_T \, d\Omega \\
&+ \int_\Omega \left(\rho_f^{k+1,m} \left(\alpha - \phi^{k+1,m}\right) \beta_s + \phi^{k+1,m} \left(\frac{\partial \rho_f}{\partial p} \right)^{k+1,m} \right) p^{k+1,m+1} P_T \, d\Omega \\
&+ \int_\Omega \Delta t \left(\rho_f^{k+1,m} \nabla \cdot \vec{q}^{\,k+1,m+1} + \vec{q}^{\,k+1,m+1} \cdot \nabla \rho_f^{k+1,m} \right) P_T \, d\Omega \\
&= \int_\Omega \rho_f^{k+1,m} \alpha \epsilon_v^{k} P_T \, d\Omega \\
&+ \int_\Omega \left(\rho_f^{k+1,m} \left(\alpha - \phi^{k+1,m}\right) \beta_s + \phi^{k+1,m} \left(\frac{\partial \rho_f}{\partial p} \right)^{k+1,m} \right) p^{k} P_T \, d\Omega \\
&+ \int_\Omega \Delta t f_f^{k+1,m} P_T \, d\Omega
\end{aligned} \tag{22}$$

and

$$\int_\Omega \left(\frac{\mu}{\kappa} \vec{q}^{\,k+1,m+1} \cdot \vec{Q}_T - p^{k+1,m+1} \nabla \cdot \vec{Q}_T \right) d\Omega = - \int_\Gamma p^{k+1,BC} \vec{Q}_T \cdot \vec{n} \, d\Gamma \tag{23}$$

and

$$\int_\Omega \boldsymbol{\sigma}^{k+1,m+1} \cdot \nabla \vec{U}_T \, d\Omega = \int_\Gamma \left(\boldsymbol{\sigma}^{k+1,BC} \cdot \vec{n} \right) \cdot \vec{U}_T \, d\Gamma \tag{24}$$

where $p^{k+1,BC}$ is the stipulated pressure boundary condition and $\boldsymbol{\sigma}^{k+1,BC}$ is the stipulated stress boundary condition. The time level and Picard iteration are written out explicitly in Eqs. (22) through (24).

To stabilize the numerical model, Eqs. (22) through (24) are solved monolithically in a mixed finite element scheme. As noted above, this approach avoids spurious, unphysical oscillations in the pressure and solid displacement solutions (Ferronato and Gambolati, 2010). Moreover, solving continuity and Darcy's law simultaneously produces a continuous and mass-conserving solution for specific discharge. While a monolithic approach complicates the numerical method compared to a staggered model (Kim et al., 2011; Kolesov et al., 2014), FEniCS can handle most of these complications automatically; thus, the benefits greatly outweigh the drawbacks.

3.2. FEniCS implementation

The FEniCS Project provides a streamlined, open-source framework for solving systems of partial differential equations using the finite element method (Alnaes et al., 2015). The software makes use of several advances in automated finite element methodologies, including DOLFIN (Logg and Wells, 2010), FFC (Kirby and Logg, 2006), FIAT (Kirby, 2004), and UFL (Alnaes et al., 2014), among others. The default linear algebra backend for FEniCS is PETSc (Abhyankar et al., 2018). The weak form of the governing equations must be supplied in a symbolic form using UFL (Unified Form Language), while the other components of FEniCS can automatically handle the mesh generation, function space definition, and finite element assembly and solving.

The poroelastic model presented here is developed with FEniCS's Python library. By making use of the internal MPI commands available in the FEniCS software, the code (including the Picard iteration) may be run in parallel with multiple processors, allowing for significantly faster computation times.

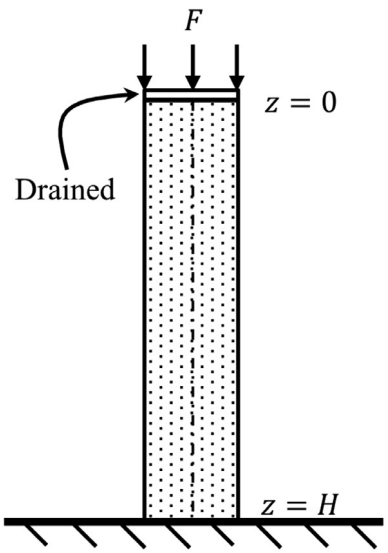

Fig. 1. Schematic of Terzaghi's one-dimensional problem, represented by a column of height H. Downward load F is applied at time t_0.

4. Model verification

The model was verified using two well-known poroelastic problems: Terzaghi's problem and Cryer's problem. Both problems have analytical solutions for the linear case, which were used to verify the linear model. The nonlinear case does not have an analytical solution for either problem, but the nonlinear model is compared to the linear model to illustrate the effect of its generalizations. Note that the poroelastic properties and problem parameters were chosen such that fluid density and porosity would vary significantly, leading to substantial discrepancies between the linear and nonlinear models. Other scenarios may very well lead to negligible differences.

4.1. Terzaghi's problem

The first benchmark problem used to verify the model is the well-known Terzaghi's problem (Terzaghi, 1925; Verruijt, 2008). Consider a one-dimensional vertical column with height H of homogeneous, fully saturated porous medium in the absence of gravity. The bottom of the column is a fixed and impervious boundary. The top of the column is a free surface allowed to drain. Initially, the undisturbed domain has zero pressure everywhere. At time t_0, a constant downward loading of F is applied on the top boundary. A two-dimensional schematic of the problem domain is seen in Fig. 1. Here, z is taken as the depth in the domain where $z = 0$ corresponds to the free surface.

Initially, the loading will induce an instantaneous increase in fluid pressure and slightly consolidate the sample. This is called the undrained response. As time progresses, fluid is allowed to drain through the top boundary and fluid pressure dissipates. This reduction in fluid pressure near the top of the domain increases the compressive effective stress felt by the porous medium, and consolidation continues. This is called the drained response. Once fluid pressure returns to zero everywhere, consolidation ceases and the sample is at steady state.

For Terzaghi's problem, boundary conditions for the top boundary are given as

$$p(z = 0, t) = 0 \tag{25}$$

$$\boldsymbol{\sigma}(z = 0, t) \cdot \vec{n} = F\hat{k} \tag{26}$$

and along the bottom as

$$\vec{q}(z = H, t) \cdot \vec{n} = 0 \tag{27}$$

Table 1
Parameters for Terzaghi's and Cryer's problems.

Parameter	Value
κ	$1 \cdot 10^{-18}$ m^2
ϕ	0.05
μ	$8.9 \cdot 10^{-4}$ Pas
β_m	$1.0 \cdot 10^{-10}$ Pa^{-1}
β_f	$4.4 \cdot 10^{-10}$ Pa^{-1}
β_s	$1.0 \cdot 10^{-11}$ Pa^{-1}
ν	0.25
F	$5.0 \cdot 10^{9}$ Pa

$$\vec{u}(z=H,t)\cdot\vec{n}=0. \tag{28}$$

Before the transient drained response, the undrained response is simulated as a single static solve with loading applied and impervious boundaries on all sides. Poroelastic properties of the porous medium and other model parameters are summarized in Table 1.

For uniaxial consolidation, the continuity equation can be decoupled from mechanics and solved analytically (Carslaw and Jaeger, 1959; Cheng, 2016; Verruijt, 2013; Wang, 2000). Mechanical equilibrium can then be solved using the pressure solution. The initial undrained response for the fluid pressure throughout the domain is given by

$$p_0 = \frac{\alpha m_v}{\alpha^2 m_v + S_\epsilon} F \tag{29}$$

where m_v is the confined compressibility of the porous medium,

$$m_v = \frac{1}{K + \frac{4}{3}G} \tag{30}$$

and S_ϵ is the drained storage coefficient,

$$S_\epsilon = (\alpha - \phi)\beta_s + \phi\beta_f. \tag{31}$$

In Eq. (31), porosity is assumed to be a constant. For fluid pressure during the drained response, the analytical solution is given by

$$p(z,t) = \frac{4}{\pi} p_0 \sum_{i=1}^{\infty} \frac{1}{2i-1} \sin\left(\frac{(2i-1)\pi}{2H} z\right) \exp\left(-\left[\frac{(2i-1)\pi}{2H}\right]^2 c_v t\right) \tag{32}$$

where c_v is the consolidation coefficient

$$c_v = \frac{\kappa}{\mu\left(\alpha^2 m_v + S_\epsilon\right)}. \tag{33}$$

To generalize the results, nondimensional variables for fluid pressure, depth, and time can be defined as: $p^* = p(z,t)/p_0$, $z^* = z/H$, and $t^* = c_v t/H^2$ respectively. As shown in Fig. 2, the fluid pressure dissipates from the initial undrained response, p_0, back to zero as fluid drains from the top boundary. Notice that the diffusion of fluid pressure through the top boundary is hastened in the nonlinear model due to the decrease in porosity and increase in fluid density during the undrained response. Both of these factors effectively increase the hydraulic diffusivity of the porous medium.

Consolidation is measured by the vertical component of solid displacement at the top boundary, where positive consolidation is downward displacement. The undrained response of consolidation is given by

$$u_{z0} = \left(m_v - \frac{\alpha^2 m_v^2}{\alpha^2 m_v + S_\epsilon}\right) FH \tag{34}$$

and the steady state consolidation is given by

$$u_{z\infty} = m_v F H. \tag{35}$$

The transient drained response of consolidation is given by

$$u_z(z=0,t)$$

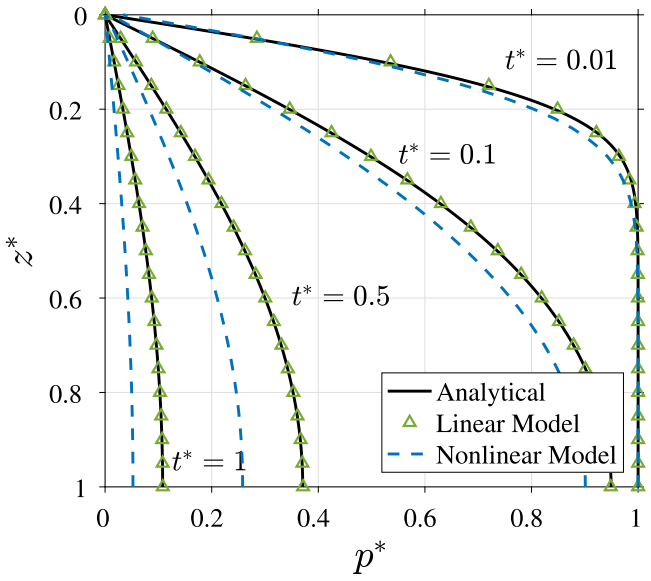

Fig. 2. Plot of nondimensional fluid pressure against nondimensional depth for various nondimensional times during simulation of Terzaghi's problem. Both linear and nonlinear models are compared to analytical solution.

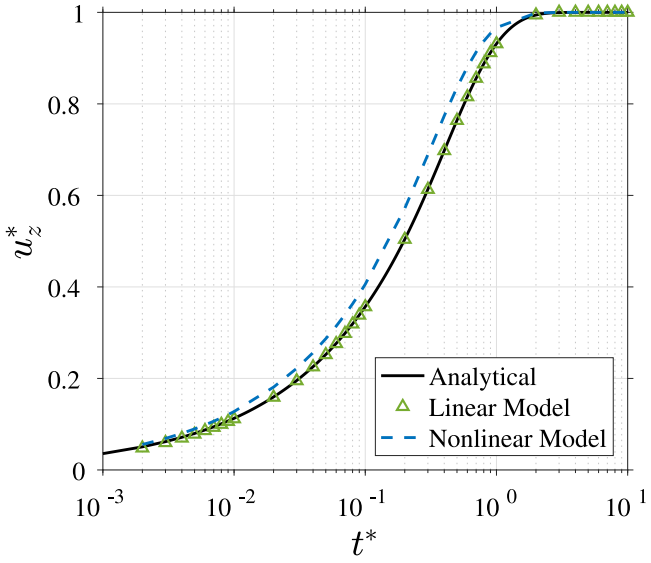

Fig. 3. Plot of nondimensional consolidation against nondimensional time for Terzaghi's problem. Both linear and nonlinear models are compared to analytical solution.

$$= -m_v F H + \frac{8\alpha m_v H}{\pi^2} p_0 \sum_{i=1}^{\infty} \frac{1}{(2i-1)^2} \exp\left(-\left[\frac{(2i-1)\pi}{2H}\right]^2 c_v t\right). \tag{36}$$

Consolidation can be nondimensionalized with $u_z^* = \left(u_z(z=0,t) - u_{z0}\right) / \left(u_{z\infty} - u_{z0}\right)$. Fig. 3 plots the nondimensional consolidation over time and clearly shows the asymptotic approach to a steady state. Notice that, since fluid pressure dissipates more quickly in the nonlinear model, the porous sample consolidates more rapidly compared to the linear model.

4.2. Cryer's problem

In fully coupled poroelasticity, one critical phenomenon that a model must be able to reproduce is the Mandel–Cryer effect (Cryer,

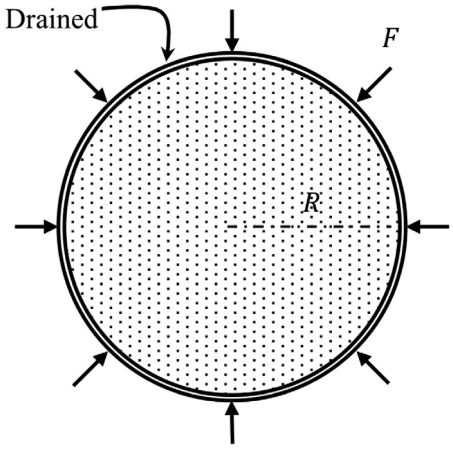

Fig. 4. Schematic of Cryer's three-dimensional problem, represented by a circle of radius R. Inward load F is applied at time t_0.

1963; Mandel, 1953; Verruijt, 2008). Exemplified in both Mandel's and Cryer's problems, the Mandel–Cryer effect is the nonmonotonic fluid pressure variation with time in response to a constant loading. This can only be replicated with a fully coupled poroelastic approach.

For Cryer's problem, consider a spherical sample of homogeneous, fully saturated porous medium with radius R centered at the origin. Initially, the sample is unperturbed and the fluid pressure is zero everywhere. At time t_0, an instantaneous radial loading F is applied on the entire pervious boundary. A two-dimensional representation of Cryer's problem is presented in Fig. 4.

As in Terzaghi's problem, the instantaneous loading induces an undrained response. The fluid pressure increases uniformly and the sample consolidates slightly. As fluid is allowed to drain through the pervious boundary, fluid pressure decreases near the edges and consolidation continues. Unlike Terzaghi's problem, though, fluid pressure at the center of the domain initially increases as drainage begins before dissipating back to zero, which is the so-called Mandel–Cryer effect.

The boundary condition for the spherical domain in FEniCS can be written as

$$p\,(r = R, t) = 0 \tag{37}$$

$$\left(\boldsymbol{\sigma} \cdot \vec{n}\right) \cdot \vec{n} = F \tag{38}$$

The traction boundary condition given in Eq. (38) is calculated for each mesh facet on the domain boundary, Γ, and included in weak form (i.e. Eq. (24)). Poroelastic properties of the porous medium and other model parameters are summarized in Table 1.

An analytical solution for Cryer's problem can be found using Laplace transforms (Verruijt, 2008). The initial undrained response for fluid pressure is

$$p_0 = \frac{\alpha F}{\alpha^2 + K S_\epsilon}. \tag{39}$$

The transient analytical solution for the fluid pressure at the origin is given by

$$p\,(r = 0, t) = \eta p_0 \sum_{i=1}^{\infty} \frac{\sin \xi_i - \xi_i}{\eta \xi_i \cos \xi_i / 2 + (\eta - 1) \sin \xi_i} \exp\left(-\frac{\xi_i^2 c_v t}{R^2}\right) \tag{40}$$

where

$$\eta = \frac{\alpha^2 + K S_\epsilon}{2 G m_v \alpha^2} \tag{41}$$

and ξ_i is the ith root of the equation

$$\left(1 - \eta \xi_i^2 / 2\right) \tan \xi_i - \xi_i = 0. \tag{42}$$

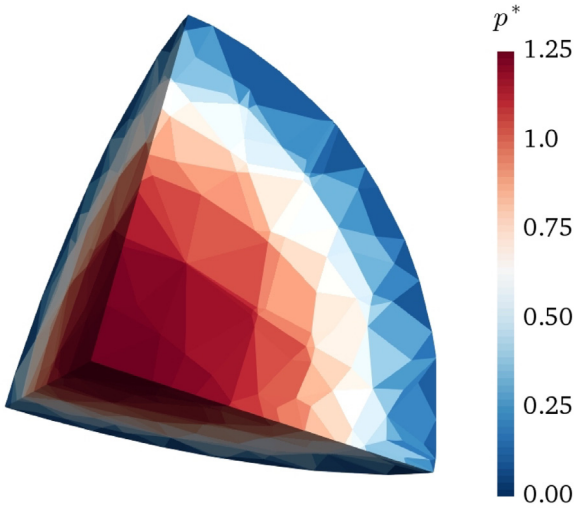

Fig. 5. Plot of nondimensional fluid pressure over a portion of spherical domain for nonlinear model.

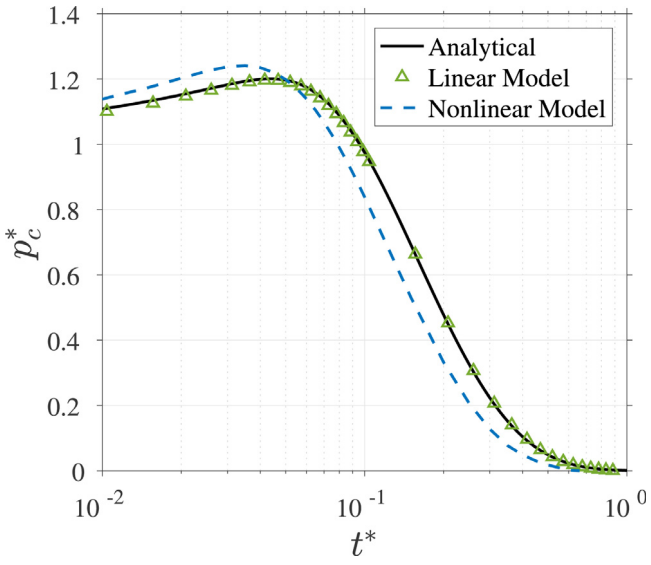

Fig. 6. Plot of nondimensional fluid pressure at sphere's center against nondimensional time for Cryer's problem. Both linear and nonlinear models are compared to analytical solution.

Nondimensionalizing fluid pressure in a similar manner as Terzaghi's problem, we define two dimensionless variables: $p^* = p/p_0$ and $p_c^* = p\,(r = 0, t)\,/p_0$. Fig. 5 shows the solution for p^* over a portion of the spherical domain for the nonlinear model. The nondimensional fluid pressure at the sphere center (p_c^*) is plotted over time in Fig. 6 for both the linear and nonlinear models. Notice the nonmonotonic variation in fluid pressure corresponding to the Mandel–Cryer effect. Fluid pressure near the center of the spherical domain initially increases with time as pressure is allowed to dissipate along the domain's edge. The nonlinear model tends to exacerbate the peak of fluid pressure and, similar to Terzaghi's problem, hasten the dissipation of the fluid pressure as fluid drains through the outer boundary.

5. Noordbergum effect

To showcase the model's ability to replicate realistic scenarios with interesting poroelastic behavior, the linear model was applied to a two-dimensional, plane strain problem of fluid extraction to reproduce

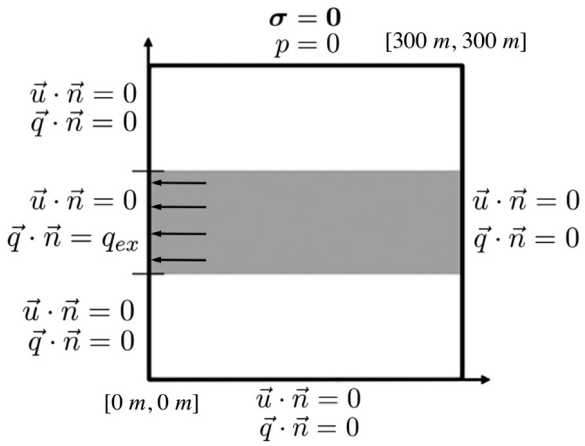

Fig. 7. Schematic of fluid extraction problem designed to recreate Noordbergum effect. Boundary conditions for fluid flow and mechanics are shown. Gray area is sand layer. White areas are clay layers.

Table 2
Parameters for fluid extraction problem.

Parameter	Sand	Clay	Constants
κ	$1 \cdot 10^{-12}$ m^2	$1 \cdot 10^{-15}$ m^2	–
ϕ	0.3	0.4	–
μ	–	–	$8.9 \cdot 10^{-4}$ Pas
β_m	$2.0 \cdot 10^{-9}$ Pa^{-1}	$2.0 \cdot 10^{-9}$ Pa^{-1}	–
β_f	–	–	$4.4 \cdot 10^{-10}$ Pa^{-1}
β_s	–	–	$1.0 \cdot 10^{-11}$ Pa^{-1}
ν	0.25	0.25	–
q_{ex}	–	–	$1.1 \cdot 10^{-4}$ cm/hr

the well-known Noordbergum effect. Here, the domain is composed of a highly permeable layer (such as sand) between two layers with low permeability (such as clay). Fluid extraction is simulated with a constant flux boundary condition on the left hand side of the highly permeable layer. The left edge of the low permeability layers, right edge of the entire domain, and the bottom boundary are impervious with roller-type mechanical boundary conditions. The top boundary represents the free surface and the water table. Note that the total stress tensor $\boldsymbol{\sigma}$ is set to zero along the top boundary, not the effective stress tensor $\boldsymbol{\sigma}'$, which is the stress tensor controlling solid deformation. Setting all components of $\boldsymbol{\sigma}$ to zero simply implies that there is no applied loading along the top boundary. A schematic of the model domain is presented in Fig. 7. The model parameters and poroelastic properties are summarized in Table 2. After one day of pumping, the pump is turned off and the left edge of the highly permeable layer is converted to a no-flux condition. Since we consider this problem to be plane strain, rather than axisymmetric, the model is only a qualitative representation of a vertically oriented pumping well.

The fluid pressure will increase in hydraulically-isolated, adjacent layers due to fluid extraction of a pumped formation (Gambolati, 1974; Hsieh, 1996; Verruijt, 1969; Wolff, 1970). This phenomenon is commonly referred to as the Noordbergum effect or "reverse water-level fluctuation" (Andreason and Brookhart, 1963). The increase in fluid pressure of the unpumped layer has been previously explained in numerous ways. In 1969, Verruijt proposed that the attraction of water in the adjacent layers towards the pumping well induces a compressive stress on the porous media, which in turn induces an increase in fluid pressure as the fluid resists compaction. This approach, however, ignores horizontal strains in the pumped formation and the transfer of stresses along the interface of the pumped and unpumped layers. Wolff (1970) showed that measured horizontal strains during a pumping test were not entirely negligible as previously thought. He suggested that shear stresses transferred from the pumped layer to unpumped layer must be inducing horizontal strains and, in turn, fluid pressure variations. Gambolati (1974) suggested that pumping generates a change in the stress state of both the pumped and unpumped layers leading to a decrease in the volume of the pore space. Assuming the fluid is relatively incompressible, this volumetric compaction will produce temporary fluid pressure increases before fluid flow causes them to dissipate (Cheng, 2016; Hsieh, 1996; Kim and Parizek, 1997; Verruijt, 2013; Wang, 2000). Other numerical studies of the Noordbergum effect include: Hsieh (1996), Rodrigues (1983), Kim and Parizek (1997), and Ferronato and Gambolati (2010).

As seen in Fig. 8, the model can indeed reproduce the Noordbergum effect during a fluid extraction simulation. Fluid pressure increases in the adjacent clay layers as fluid is being extracted from the central sand layer. The pattern of the Noordbergum effect in this simulation agrees well with the results of Hsieh (1996) and Kim and Parizek (1997). Once pumping ceases, fluid pressures tend back to the initial condition throughout the domain as the elastic body recovers its original shape and fluid pressure perturbations dissipate through fluid flow.

Contrary to prior studies of the Noordbergum effect, we suggest an alternate physical mechanism creating the increase in fluid pressure: induced strain gradients. In this simulation, both the fluid and solid grains are essentially incompressible over the range of expected pressure changes. Any volumetric strain, therefore, must be due to the rearrangement of soil grains and a corresponding fluid flow. In the clay layers, though, fluid flow is greatly inhibited by the layer's low permeability. Pressure gradients in the low permeability layers are not large enough to induce significant fluid flow. Examining Eq. (10) shows that, in this case, every term is effectively zero, including the time

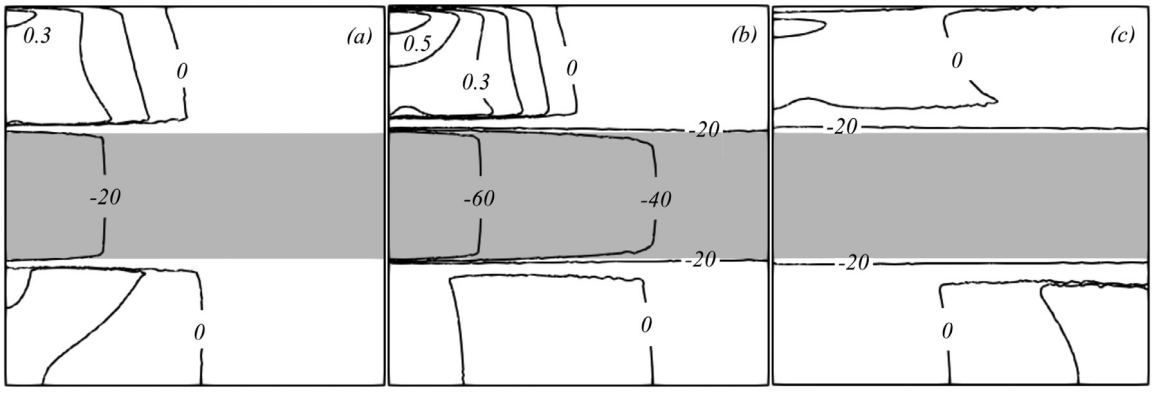

Fig. 8. Model results for fluid pressure of fluid extraction simulation showing Noordbergum effect at three times: (a) t = 6 hr, (b) t = 24 hr, and (c) t = 48 hr. Notice unequal contour spacing. Fluid pressure units are in Pascals. Gray area is sand layer. White areas are clay layers.

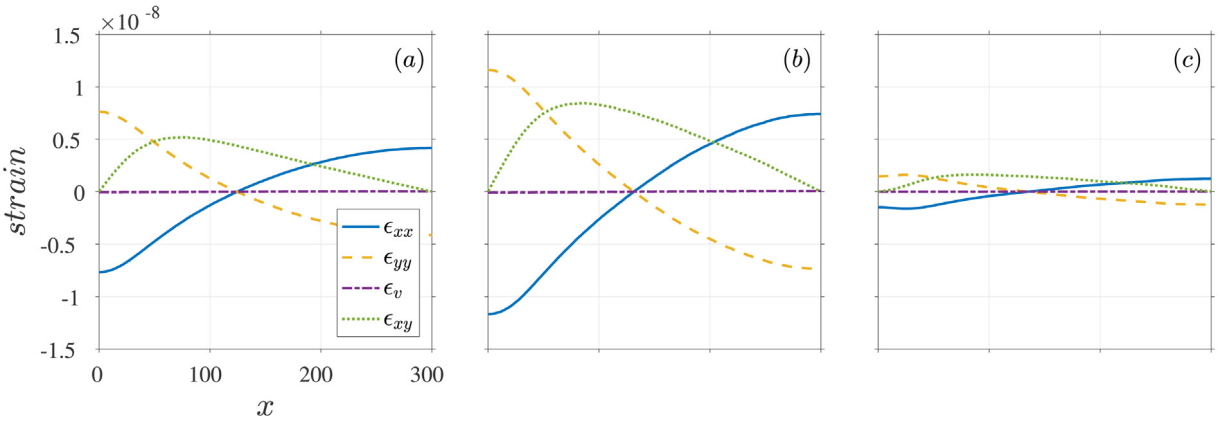

Fig. 9. Volumetric strain ϵ_v and its components ϵ_{xx} and ϵ_{yy} along centerline of upper layer at various times: (a) $t = 6$ hr, (b) $t = 24$ hr, and (c) $t = 48$ hr. For completeness, shear strain ϵ_{xy} is also plotted.

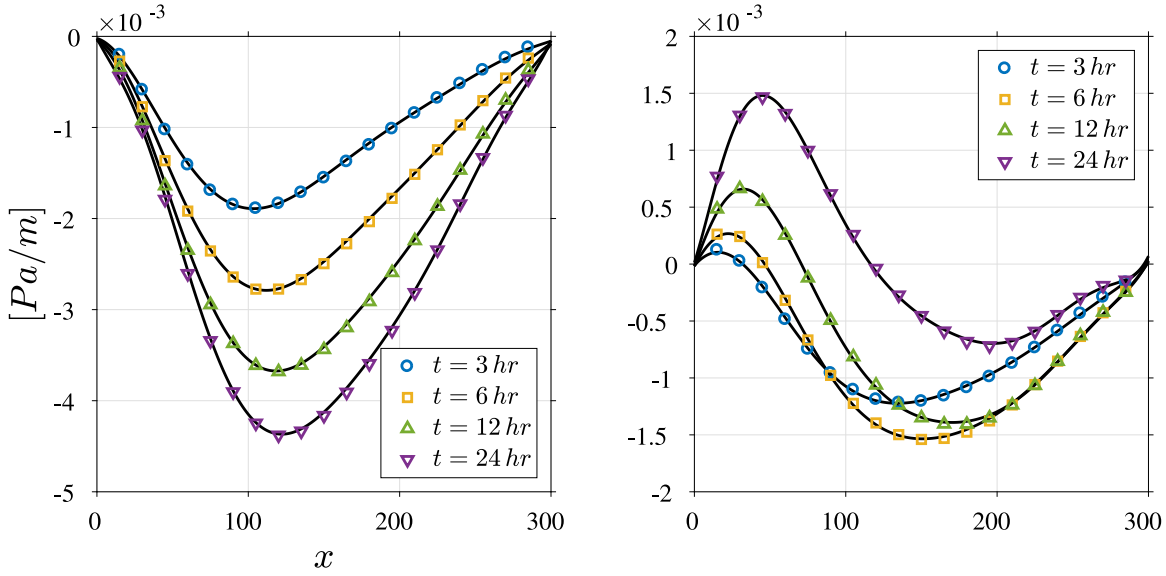

Fig. 10. Averaged model values for left-hand-side (solid black line) and right-hand-side (colored markers) of Eqs. (43) and (44) along centerline of upper layer at various times: (left) Eq. (43) and (right) Eq. (44).

derivative of the volumetric strain. Thus, volumetric strain in the clay layers should not develop during the simulation. Fig. 9 indicates this is indeed the case by plotting the volumetric strain and its principal components (ϵ_{xx} and ϵ_{yy}) along the horizontal centerline of the upper layer. For the sake of completeness and comparison, the shear strain ϵ_{xy} is also shown in Fig. 9.

Relying on the current explanation of the Noordbergum effect would lead one to assume that fluid pressures should not increase in the absence of volumetric strains, yet within our fully poroelastic modeling framework, fluid pressure is nonetheless increasing. Inspecting the governing equations for mechanical deformation and their coupling with fluid pressure enlightens us to the cause of this unexpected result. Substituting Eq. (12) and (13) into Eq. (11) and using $\epsilon_v = 0$, the spatial derivatives of fluid pressure can be expressed as

$$\alpha \frac{\partial p}{\partial x} = 2G \left(\frac{\partial \epsilon_{xx}}{\partial x} + \frac{\partial \epsilon_{xy}}{\partial y} \right) \tag{43}$$

$$\alpha \frac{\partial p}{\partial y} = 2G \left(\frac{\partial \epsilon_{yx}}{\partial x} + \frac{\partial \epsilon_{yy}}{\partial y} \right) \tag{44}$$

where ϵ_{ij} are the components of the strain tensor. Eqs. (43) and (44) suggest that strain gradients, rather than volumetric strains, are generating variations in fluid pressure. To confirm the accuracy of Eqs. (43) and (44), we plot the averaged model values of left hand side (LHS) and right hand side (RHS) of each equation in Fig. 10 at various times during the simulation along the centerline of the upper layer where the Noordbergum effect occurred. Fig. 10 clearly shows that the LHS and RHS of Eqs. (43) and (44) match well during the pumping simulation, indicating that these equations appropriately describe the model's behavior and, hence, the generation of the Noordbergum effect. The expressions given in Eqs. (43) and (44) are only valid for the two-dimensional, plane strain problem posed here. The exact form of these expressions would differ when considering either axisymmetric or three-dimensional problems. Still, there would be a lack of fluid flow and solid or fluid compression in the low permeability layers in axisymmetric or three-dimensional simulations, leading to a lack of volumetric strain. It is likely that strain gradients of some form would remain the underlying cause of the Noordbergum effect in these cases.

Wolff (1970) experimentally discovered that horizontal surface strains during pumping tend to reverse from compression to tension at some distance away from the pumping location. The author explained this behavior by the presence of a river nearby the study site, which

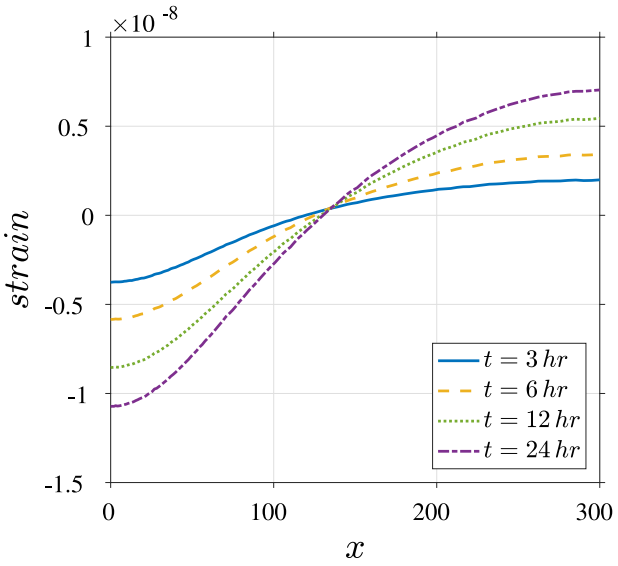

Fig. 11. Horizontal strain along ground surface at various times during simulated pumping.

was represented as an infinite line source in the author's solution. Our poroelastic model, however, can replicate this behavior without necessitating any other fluid sources or sinks other than the pumping well. Fig. 11 shows the horizontal strains along the ground surface of the model domain at various times during the simulation. Notice the expected reversal of strain from compression to tension. The magnitude of strains is considerably lower than those measured in the field by Wolff (1970), likely due to different pumping rates and poroelastic parameters between the two scenarios.

6. Conclusions

To contribute to the open-source geoscientific modeling community, we present here a model for linear and nonlinear poroelasticity built within FEniCS, a finite element method framework. Advances in automated solution techniques for the finite element method, such as FEniCS, provide the user with a streamlined approach for solving systems of partial differential equations compared to traditional model development. Unlike prebuilt models (e.g. TOUGH-FLAC or PFLOTRAN), the model presented here also gives the user a great deal of control over many model components. For these reasons, FEniCS has garnered recent interest from the geoscientific community. We follow this trend by presenting a FEniCS model for poroelasticity. The full model code, along with verification problems and a general user guide, is freely available as a Github repository.

The model is capable of a standard linear poroelastic formulation, which is used to verify the model behavior by solving well-known benchmark problems. Additionally, the model includes a generalized nonlinear poroelastic formulation by employing a variable fluid density and porosity. Here, the porosity relationship is based on solid continuity. We show that this choice leads to an internally consistent mathematical model, unlike other popular porosity relationships. One major advantage of this model is the flexibility of the FEniCS framework, allowing the model user to easily apply various generalizations such as inelastic constitutive relationships or a highly compressible equation of state. It is possible to extend the formulation to multiphase flow problems, for which the user would need to include additional equations for the new fluid phases in the weak form, along with the appropriate constitutive relationships and coupling terms with mechanics. Multiphase flow problems, however, might introduce additional numerical challenges. Finally, the model employs a mixed finite element technique to solve the system monolithically, which has been shown to increase numerical stability and avoid poroelastic "locking".

The model was applied to a two-dimensional, plane strain problem of fluid extraction in order to study the Noordbergum effect, which is only replicable in a fully poroelastic formulation. Contrary to prior findings, the model shows clearly that strain gradients – rather than volumetric strains – are responsible for inducing the Noordbergum effect. This showcase problem highlights the flexibility and usefulness of the poroelastic model. Other potential applications for the model – both the linear and nonlinear formulations – include studies of injection-induced or reservoir-induced seismicity, geological carbon sequestration, subsurface remediation, ground surface displacement due to pumping operations, or the analysis of pumping test results and subsurface characterization. Although the showcase problem presented here is two-dimensional, the model is perfectly capable of three-dimensional problems (with sufficient computational resources) as exemplified here by Cryer's problem.

Code availability

The full code of the poroelastic model presented here is freely available along with a general user guide at: https://github.com/ryanhaagenson/Generalized_Poroelastic_Model_FEniCS. The developer, Ryan Haagenson, can be contacted at ryan.haagenson@colorado.edu or at 1111 Engineering Dr, 422 UCB, Boulder, CO, 80309, USA. The code was developed and tested with the Python module of FEniCS version 2017.2.0 through the prebuilt Docker image. Please refer to https://fenicsproject.org for full system requirements.

Declaration of competing interest

The authors declare that they have no known competing financial interests or personal relationships that could have appeared to influence the work reported in this paper.

CRediT authorship contribution statement

Ryan Haagenson: Conceptualization, Formal analysis, Investigation, Software, Validation, Visualization, Writing - original draft. **Harihar Rajaram:** Conceptualization, Funding acquisition, Project administration, Resources, Supervision, Writing - review & editing. **Jeffery Allen:** Investigation, Software, Writing - review & editing.

Acknowledgments

This work was financially supported by the National Science Foundation, USA Hazards SEES project EAR 1520846 at the University of Colorado Boulder and Los Alamos National Laboratory, USA (Center for Space and Earth Science and subcontract 437948 to the University of Colorado from LDRD Project 20170103DR). Also, we would like to thank Daniel Birdsell (now at ETH Zürich) for the numerous, insightful conversations about the theory of poroelasticity. We would like to thank two anonymous reviewers for their generous help in improving the quality of this paper.

References

Abhyankar, S., Brown, J., Constantinescu, E.M., Ghosh, D., Smith, B.F., Zhang, H., 2018. PETSc/TS: a modern scalable ODE/DAE solver library. ArXiv preprint.

Adams, R.A., Fournier, J., 2003. Sobolev spaces. In: Pure and Applied Mathematics, vol. 140, second ed. Academic Press, Boston, MA, p. 305.

Alnaes, M., Blechta, J., Hake, J., Johansson, A., Kehlet, B., Logg, A., Richardson, C., Ring, J., Rognes, M.E., Wells, G.N., 2015. The fenics project version 1.5. Arch. Numer. Softw. 3 (100).

Alnaes, M., Logg, A., Ølgaard, K.B., Rognes, M.E., Wells, G.N., 2014. Unified form language: a domain-specific language for weak formulations of partial differential equations. ACM Trans. Math. Software 40 (9).

Andreason, G.F., Brookhart, J.W., 1963. Reverse water-level fluctuations. In: Methods of Collecting and Interpreting Ground-Water Data. United States Geological Survey Water-Supply Paper 1544-H. pp. 30–35.
Biot, M.A., 1941. General theory of three-dimensional consolidation. J. Appl. Phys. 12, 155–164.
Biot, M.A., 1962. Mechanics of deformation and acoustic propagation in porous media. J. Appl. Phys. 33 (4), 1482–1498.
Biot, M.A., Willis, D.G., 1957. The elastic coefficients of the theory of consolidation. J. Appl. Mech. 24, 594–601.
Brezzi, F., Douglas, Jr., J., Marini, L.D., 1985. Two families of mixed finite elements for second order elliptic problems. Numer. Math. 47 (2), 217–235.
Brezzi, F., Fortin, M., 1991. Mixed and Hybrid Finite Element Methods. Springer-Verlag, New York, NY, p. 352.
Cappa, F., Rutqvist, J., 2011. Impact of CO_2 geological sequestration on the nucleation of earthquakes. Geophys. Res. Lett. 38.
Carslaw, H.S., Jaeger, J.C., 1959. Conduction of Heat in Solids, second ed. Oxford Printing Press, Oxford, UK, p. 510.
Chang, K.W., Segall, P., 2016. Injection-induced seismicity on basement faults including poroelastic stressing. J. Geophys. Res.: Solid Earth 121, 2708–2726.
Cheng, A.H.-D., 2016. Poroelasticity: Theory and Applications of Transport in Porous Media, vol. 27. Springer International, Switzerland, p. 877.
Coussy, O., 2004. Poromechanics. Wiley, Chichester, UK, p. 312.
Cryer, C.W., 1963. A comparison of the three-dimensional consolidation theories of Biot and Terzaghi. Quart. J. Mech. Appl. Math. 16, 401–412.
Detournay, D., Cheng, A.H.-D., 1993. Fundamentals of poroelasticity. In: Rock Engineering: Principles, Practice and Projects, vol. II. Pergamon Press, Oxford, pp. 133–171.
Fall, M., Nasir, O., Nguyen, T.S., 2014. A coupled hydro-mechanical model for simulation of gas migration in host sedimentary rocks for nuclear waste repositories. Eng. Geol. 176, 24–44.
Fang, Y., Nguyen, B.N., Carroll, K., Xu, Z., Yabusaki, S.B., Scheibe, T.D., Bonneville, A., 2013. Development of a coupled therm-hydro-mechanical model in discontinuous media for carbon sequestration. Int. J. Rock Mech. Min. Sci. 62, 138–147.
Ferronato, M., Gambolati, G., 2010. A fully coupled 3-D mixed finite element model of Biot consolidation. J. Comput. Phys. 229, 4813–4830.
Gambolati, G., 1974. Second-order theory of flow in three-dimensional deforming media. Water Resour. Res. 10 (6), 1217–1228.
Gambolati, G., Teatini, P., Baú, D., Ferronato, M., 2000. Importance of poroelastic coupling in dynamically active aquifers of the Po river basin, Italy. Water Resour. Res. 36 (9), 2442–2459.
Gaston, D., Newman, C., Hansen, G., Lebrun-Grandié, D., 2009. MOOSE: A parallel computational framework for coupled systems of nonlinear equations. Nucl. Eng. Des. 239 (10), 1768–1778.
Geertsma, J., 1957. A remark of the analogy between thermoelasticity and the elasticity of saturated porous media. J. Mech. Phys. Solids 6, 13–16.
Hou, Z., Yang, G., Taron, J., Gorke, U.J., Kolditz, O., 2012. Thermo-hydro-mechanical modeling of carbon dioxide injection for enhanced gas=recovery (CO_2-EGR): a benchmarking study for code comparison. Environ. Earth Sci. 67, 549–561.
Hsieh, P., 1996. Deformation-induced changes in hydraulic head during ground-water withdrawal. Ground Water 34 (6), 1082–1089.
Karra, S., Bisht, G., Lichtner, P.C., Hammond, G.E., 2013. Coupling geomechanics with flow and reactive transport in PFLOTRAN for subsurface applications. In: Proceedings of the American Geophysical Union Fall Meeting 2013, San Fransisco, CA, USA. Abstract id: H21E-1106.
Kim, J., Parizek, R., 1997. Numerical simulation of the Noordbergum effect resulting from groundwater pumping in a layered aquifer system. J. Hydrol. 202, 231–243.
Kim, J., Tchelepi, H.A., Juanes, R., 2011. Stability and convergence of sequential methods for coupled flow and geomechanics: fixed-stress and fixed-strain splits. Comput. Methods Appl. Mech. Engrg. 200, 1591–1606.
Kirby, R.C., 2004. FIAT: a new paradigm for computing finite element basis functions. ACM Trans. Math. Software 30, 502–516.
Kirby, R.C., Logg, A., 2006. A compiler for variational forms. ACM Trans. Math. Software 32.
Kirby, R.C., Logg, A., Rognes, M.E., Terrel, A.R., 2012. Common and unusual finite elements. In: Automated Solution of Differential Equations By the Finite Element Method. Springer, Berlin, Germany, pp. 91–116.
Kolesov, A.E., Vabishchevich, P.N., Vasilyeva, M.V., 2014. Splitting schemes for poroelasticity and thermoelasticity problems. Comput. Math. Appl. 67, 2185–2198.
Liu, Q., Cheng, Y., Zhou, H., Guo, P., An, F., Chen, H., 2015. A mathematical model of coupled gas flow and coal deformation with gas diffusion and Klinkenberg effects. Rock Mech. Rock Eng. 48, 1163–1180.
Logg, A., Wells, G.N., 2010. DOLFIN: automated finite element computing. ACM Trans. Math. Software 32 (20).
Mandel, J., 1953. Consolidation des sols. Géotechnique 7, 287–299.
Palmer, I., Mansoori, J., 1998. How permeability depends on stress and pore pressure in coalbeds: a new model. Soc. Petrol. Eng. Reserv. Eval. Eng. 1 (06).
Rodrigues, J.D., 1983. The Noordbergum effect and characterization of aquitards at the Rio Maior mining project. Groundwater 21 (2), 200–207.
Rutqvist, J., 2010. Status of the TOUGH-FLAC simulator and recent applications related to coupled fluid flow and crustal deformations. Comput. Geosci. 37, 739–750.
Rutqvist, J., Boergesson, L., Chijimatsu, M., Kobayashi, L., Jing, L., Nguyen, T.S., Noorishad, J., Tsang, C.F., 2001. Thermohydromechanics of partially saturated geological media: governing equations and formulation of four finite element, methods. Int. J. Rock Mech. Min. Sci. 38, 105–127.
Settari, A., Mourits, F.M., 1998. A coupled reservoir and geomechanical simulation system. Soc. Petrol. Eng. J. 3.
Srinivasan, S., Rajagopal, K.R., 2016. On the flow of fluids through inhomogeneous porous media due to high pressure gradients. Int. J. Non-Linear Mech. 78, 112–120.
Terzaghi, K., 1925. Erdbaumechanik auf Bodenphysikalischen Grudlagen, Deuticke, Leipzig, Germany.
Traverso, L., Phillip, T.N., Yang, Y., 2013. Mixed finite element methods for groundwater flow in heterogeneous aquifers. Comput. & Fluids 88, 60–80.
Unwin, H.J.T., Wells, G.N., Woods, A.W., 2016. CO_2 dissolution in a background hydrological flow. J. Fluid Mech. 789, 768–784.
Verruijt, A., 1969. Elastic storage of aquifers. In: Flow Through Porous Media. Academic Press, New York, NY, pp. 331–376.
Verruijt, A., 2008. Consolidation of soils. In: Encyclopedia of Hydrological Sciences. John Wiley & Sons, Ltd., Chichester, UK.
Verruijt, A., 2013. Theory and Problems of Poroelasticity, first ed. p. 259, n.p.: Author.
Vilarrasa, V., Olivella, S., Carrera, J., Rutqvist, J., 2014. Long term impacts of cold CO_2 injection on the caprock integrity. Int. J. Greenhouse Gas Control 24, 1–13.
Vilarrasa, V., Silva, O., Carrera, J., Olivella, S., 2013. Liquid CO_2 injection for geological storage in deep saline aquifers. Int. J. Greenhouse Gas Control 14, 84–96.
Wang, H.F., 2000. Theory of Linear Poroelasticity with Applications To Geomechanics and Hydrogeology, first ed. Princeton University Press, Princeton, NJ, p. 304.
Wolff, R.G., 1970. Relationship between horizontal strain near a well and reverse water level fluctuation. Water Resour. Res. 6, 1721–1728.
Wood, D.M., 1991. Soil Behaviour and Critical State Soil Mechanics, first ed. Cambridge University Press, Cambridge, UK, p. 450.
Zhang, H., Liu, J., Elsworth, D., 2008. How sorption-induced matrix deformation affects gas flow in coal seams: A new FE model. Int. J. Rock Mech. Min. Sci. 45, 1226–1236.
Zhang, C., Zarrouk, S.J., Archer, R., 2015. Development of a fully coupled flow-geomechanics simulator for flow in saturated porous media. In: Proceedings of the International Conference on Computational Methods, Auckland, New Zealand. Abstract id: ICCM2015.
Zhang, C., Zarrouk, S.J., Archer, R., 2016. A mixed finite element solver for natural convection in porous media using automated solution techniques. Comput. Geosci. 96, 181–192.
Zoback, M.D., 2010. Reservoir Geomechanics, first ed. Cambridge University Press, Cambridge, UK, p. 461.